Chemosphere 280 (2021) 130734

Contents lists available at ScienceDirect

Chemosphere

journal homepage: www.elsevier.com/locate/chemosphere

The Z-scheme NH_2-UiO-66/PTCDA composite for enhanced photocatalytic Cr(VI) reduction under low-power LED visible light

Xian Wei [a], Chong-Chen Wang [a,*], Yang Li [a], Peng Wang [a], Qi Wei [b]

[a] Beijing Key Laboratory of Functional Materials for Building Structure and Environment Remediation, Beijing University of Civil Engineering and Architecture, Beijing, 100044, PR China

[b] College of Materials Science and Engineering, Beijing University of Technology, Beijing, 100124, China

ARTICLE INFO

Handling Editor: Jun Huang

Keywords:
NH_2-UiO-66
3,4,9,10-Perylenetetracarboxylic dianhydride
Z-Scheme
Photocatalytic Cr(VI) reduction
DFT calculation

ABSTRACT

Series Z-scheme NH_2-UiO-66/PTCDA (NU100P*X*) composites constructed from NH_2-UiO-66 and PTCDA (3,4,9,10-perylenetetracarboxylic dianhydride) were obtained by simple ball-milling method. The photocatalytic Cr(VI) reduction activities of the NU100P*X* composites were conducted upon the irradiation of low power LED visible light. The results revealed that the introduction of a small amount of PTCDA on the surface of NH_2-UiO-66 could broaden the light absorption range and boost the separation of photo-induced charge carriers to promote the photocatalysis efficiency. The influence factors toward photocatalytic Cr(VI) cleanup performances of NU100P10 like pH, initial Cr(VI) concentrations, the impacts of small organic acids as hole capture agents along with various co-existing foreign matters were clarified. After 5 runs' adsorption-photoreduction towards Cr(VI), the NU100P10 still exhibited superior reduction activity and reusability. The Z-scheme mechanism of photocatalytic Cr(VI) removal over NU100P10 was put forward and certificated by electrochemical experiment, ESR (electron spin resonance) test, XPS determination, photo-deposition and DFT (density functional theory) calculation.

1. Introduction

Heavy metals and pharmaceuticals and personal care products (PPCPs) are two common pollutants in water (Palansooriya et al., 2020; Chen et al., 2021). Hexavalent chromium (Cr(VI)) is a potentially toxic pollutant from natural processes like soil and groundwater as well as human activities like the steel, electroplating, and leather industries (Li et al., 2020a; Xia et al., 2020). Due to the ecological risk and biological carcinogenicity, the elimination of Cr(VI) pollution is getting increasing attention. Recently, the photocatalytic reduction is a relatively new technique for the removal of dissolved Cr(VI) (Wang et al., 2015, 2016a; Wei et al., 2017; Zhao et al., 2020). Comparing with ion exchange and chemical adsorption, photocatalysis is highly efficient and green (Galán et al., 2005; Jiang et al., 2014).

As one of the functional materials consisting of inorganic metal-oxo clusters connected by organic linkers, metal organic frameworks (MOFs) have attracted increasing attentions owing to their merits like abundant active sites, various functional groups and facile post-synthetic modification (Dhakshinamoorthy et al., 2018; Yu et al., 2019). UiO-66 and NH_2-UiO-66 with considerable surface area and excellent chemical stability were widely studied in the field of adsorption (Wang et al., 2017b; Xu et al., 2018a; Daradmare et al., 2021), catalysis (photocatalysis) (Du et al., 2019a), gas adsorption/separation (Weirsum et al., 2011), medical (Zhang et al., 2020b). Especially, UiO-66 and NH_2-UiO-66 along with their composites displayed outstanding photocatalysis activities toward elimination of Cr(VI) (Yi et al., 2019a; Zhou et al., 2019) and organic pollutants (Li et al., 2020b; Zhou et al., 2020). To further enhance the stability of MOFs and simultaneously boost the separation of photo-induced electron-hole, some conducting polymers like polyaniline (PANI) were adopted to modify MIL-100(Fe) (Chen et al., 2020c) and MIL-88A(Fe) (Chen et al., 2020a) for improving the photocatalysis activity. As a metal-free semiconductor photocatalyst, 3,4,9,10-perylenetetracarboxylic dianhydride (PTCDA) with narrow-bandgap ($E \approx 2.0$ eV), has been demonstrated to accomplish photocatalytic O_2 generation and H_2 evolution (Wang et al., 2016b; Ye et al., 2018; Sukhanova et al., 2020). In addition, PTCDA was selected to fabricate direct Z-scheme PTCDA/g-C_3N_4 photocatalyst based on interfacial strong interaction (Yuan et al., 2020). As well, PTCDA-ZnO (Radhika and Thomas, 2017) and PI (perylene imide)-modified NH_2-UiO-66(Zr) composite (Wang et al., 2020b) were fabricated to

* Corresponding author.
E-mail addresses: wangchongchen@bucea.edu.cn, chongchenwang@126.com (C.-C. Wang).

https://doi.org/10.1016/j.chemosphere.2021.130734
Received 18 February 2021; Received in revised form 21 April 2021; Accepted 25 April 2021
Available online 4 May 2021
0045-6535/© 2021 Elsevier Ltd. All rights reserved.

accomplish enhanced photocatalytic performances. Especially, Ma and coworkers synthesized PI-modified NH_2-UiO-66 via the amidation reaction between PTCDA and the amino groups attached on NH_2-UiO-66. The PI-modified NH_2-UiO-66 demonstrated boosting photocatalytic tetracycline decomposition activity under visible-light provided by 300 W Xe lamp. However, the fabrication procedure of PI-modified NH_2-UiO-66 was too complicated.

Our research group proposed that ball-milling process is a facile and effective method to construct MOF-related composites like g-C_3N_4/BUC-21 (Yi et al., 2019b), g-C_3N_4/UiO-66 (Yi et al., 2019a), g-C_3N_4/MIL-100 (Fe) (Du et al., 2019b), PANI/MIL-100(Fe) (Chen et al., 2020c), $Bi_{12}O_{17}Cl_2$/MIL-100(Fe) (Zhao et al., 2020), WO_3/MIL-100(Fe) (Wang et al., 2020a), N–$K_2Ti_4O_9$/BUC-21 (Wang et al., 2021), and S–TiO_2/UiO-66-NH_2 (Li et al., 2020b), in which the ball-milling treatment can even create new interfaces between MOFs and the secondary component (Chen et al., 2020b). Within this paper, series NH_2-UiO-66/PTCDA composites were prepared by simple ball-milling (Scheme 1). Then the excellent Cr(VI) reduction under low-power LED visible light could be achieved over NU100P*X* composites. As well, the possible mechanism of Cr(VI) removal was given and proved by both DFT calculation and the corresponding tests.

2. Experimental

2.1. Preparation of NH_2-UiO-66/PTCDA composites

The NH_2-UiO-66 was hydrothermally synthesized according to the method reported in previous report with minor modification (Zhou et al., 2019). The detailed operation steps were given in the Supplementary Information (SI). The PTCDA was obtained by commercial purchase.

The NH_2-UiO-66/PTCDA composites were prepared using ball-milling treatment (30 Hz, 20 min). The composites were named as NU100P*X* (the letters "NU" and "P" are abbreviated for NH_2-UiO-66 and PTCDA. The "100" and "*X*" are the mass ratios of NH_2-UiO-66 and PTCDA in the composites, respectively).

2.2. Photocatalytic tests

The photocatalytic performances of composites were evaluated by reduction of Cr(VI) with C_0 being 10.0 mg L^{-1} under a low 25 W LED light. And the light spectrum was shown in Fig. S1. The photocatalyst (375.0 mg L^{-1}) was dispersed into $K_2Cr_2O_7$ aqueous solution (80 mL). The equilibrium of adsorption-desorption was achieved with magnetic stirring for 1 h in the dark environment, and then irradiated by the visible light. The method of diphenylcarbazide (DPC) (Auto Analyzer 3) was used to determine the concentration of the residual Cr(VI). The picture of Auto Analyzer 3 was given in Fig. S2.

3. Results and discussion

3.1. Characterizations

The powder X-ray diffraction (PXRD) patterns of NH_2-UiO-66, PTCDA, and series NH_2-UiO-66/PTCDA (NU100P*X*) composites were displayed in Fig. 1a. Obviously, the PXRD patterns of NH_2-UiO-66 were the same as the simulated patterns from the CIF file (CCDC 1405751) and the related references (Li et al., 2020b). As well, the PXRD patterns of commercialized PTCDA were well matched with the previous literature (Wang et al., 2018). In the PXRD patterns of NH_2-UiO-66/PTCDA (NU100P*X*), the characteristic PXRD peaks of NH_2-UiO-66 could be discovered obviously. The characteristic PXRD peaks of PTCDA could not be seen due to the small dosage in the obtained composites. In FTIR spectra (Fig. 1b), for the pure NH_2-UiO-66, the absorption peaks at 1578.28 cm^{-1} and 1385.76 cm^{-1} belonged to the carboxylic functional groups in the BDC–NH_2 ligands, and the peaks between 600 and 800 cm^{-1} were ascribed to Zr–O_2 as vertical and horizontal mode scaling (Xu et al., 2018b). The spectrum of single NH_2-UiO-66 was shown in Fig. S3. For the single PTCDA, the peaks at 1592.54 cm^{-1} and 1300.80 cm^{-1} attributed to the aromatic rings in the PTCDA molecules, and the other broad absorption band at 1758.84 cm^{-1} corresponded to the carbonyl (C═O) (Yuan et al., 2020). The NU100P*X* samples exhibited the characteristic FTIR absorption peaks of both NH_2-UiO-66 and PTCDA, and the characteristic adsorption peaks of NH_2-UiO-66 at 600–800 cm^{-1} decreased due to the addition of PTCDA (Li et al., 2020b). As well, with the increase of PTCDA contents, the characteristic peaks of PTCDA at 809 cm^{-1} increased obviously. In our work, no characteristic peaks corresponding to the imine ring were observed in the composites, indicating that the composites obtained from ball milling treatment are formed by PTCDA and NH_2-UiO-66 rather than surface modification.

The UV–vis diffuse reflectance spectra (UV–vis DRS) of NH_2-UiO-66, PTCDA and NU100P*X* were displayed in Fig. 1c. The E_g value (band gap energy) was calculated according to Eq. (1) (Butler, 1977; Zhang et al., 2017; Jia et al., 2020).

$$\alpha h\nu = A\left(h\nu - E_g\right)^{n/2} \quad (1)$$

where α, h and ν are the diffuse absorption coefficient, the light constant, and the frequency, respectively. *n* is judged by the optical transition type of the semiconductor (indirect ($n = 4$) or direct ($n = 1$)). In this study, *n* is assigned as 4 (Li et al., 2015; Yi et al., 2019a). NH_2-UiO-66 and PTCDA showed absorption edges at 418 nm with E_g being ca. 2.97 eV and 602

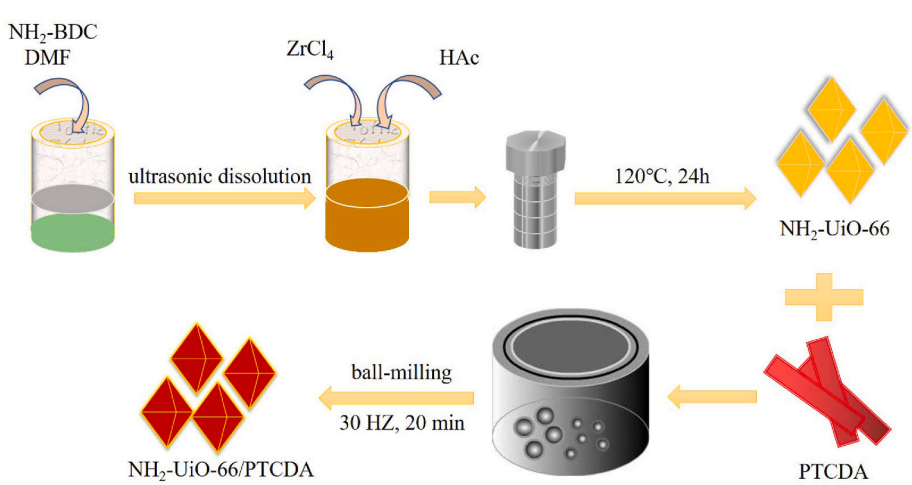

Scheme 1. Preparation diagram of the NH_2-UiO-66/PTCDA composites.

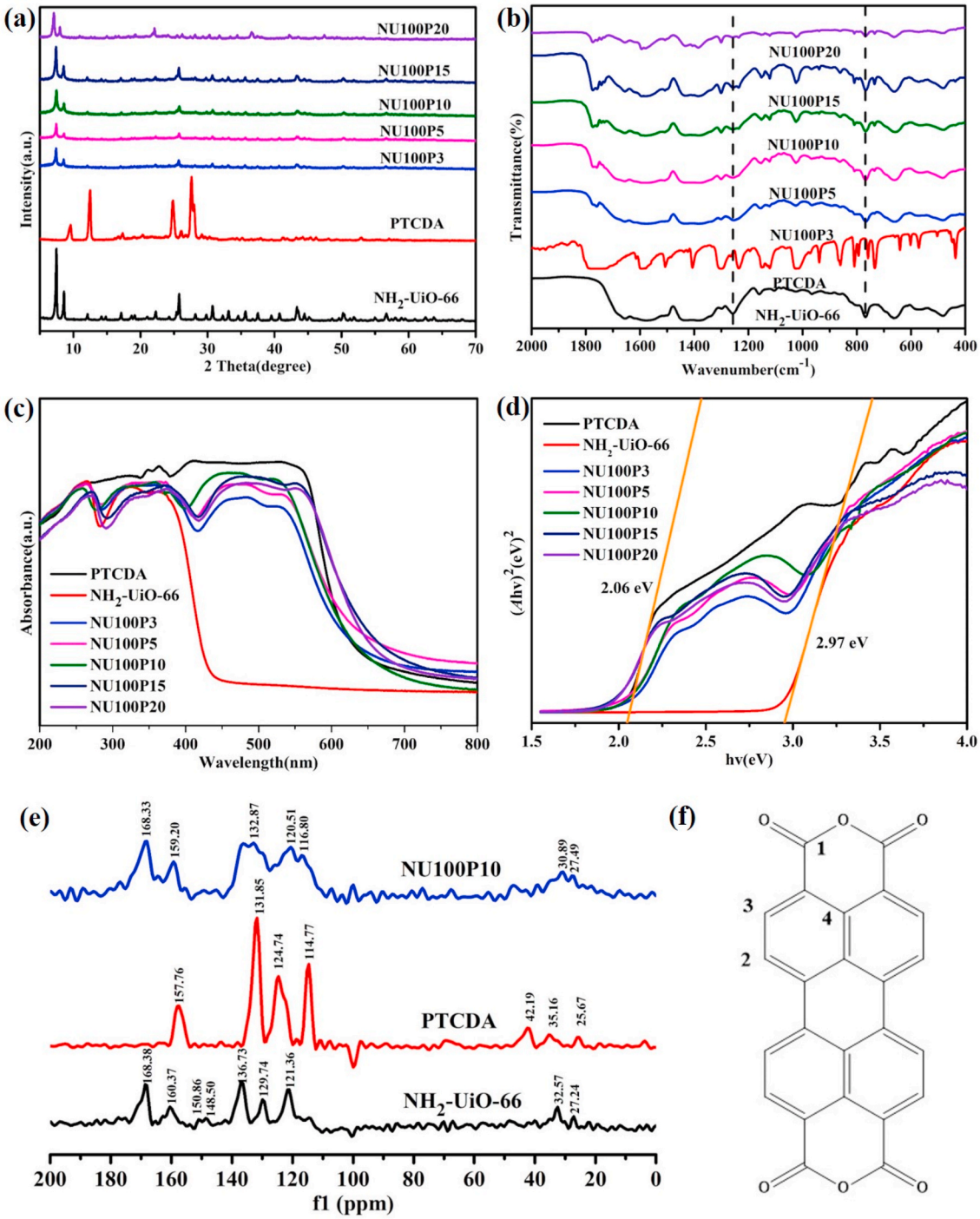

Fig. 1. (a) The XRD patterns, (b) the FTIR spectra, (c) the UV–vis DRS and (d) E_g plots of the NH_2-UiO-66, PTCDA and NU100P*X* composites. (e) The ^{13}C NMR spectra of NH_2-UiO-66, PTCDA and NU100P10 and (f) Chemical structure of PTCDA.

nm with E_g being 2.06 eV (Fig. 1d) (Wang et al., 2016b; Hu et al., 2019), respectively. Compared with single NH_2-UiO-66, the absorption range of NU100P*X* exhibited apparent red shift, implying that NU100P*X* composites could be excited by a wider range of visible light.

The results of solid high-resolution NMR (^{13}C NMR) spectra are well consistent with the FTIR results. After compounding with PTCDA, the chemical shifts values (δ value) of the C atoms on benzene ring belongs to NH_2-UiO-66 shift to low field (Zhu et al., 2019). As shown in Fig. 1e and f, the 157 ppm band of PTCDA corresponds to the carbon atoms of carbonyl double bonds in anhydride groups (#1 position in Fig. 1f), and the 131 ppm peak can be ascribed to the carbon atoms of the #2 position in Fig. 1f. In the NMR spectra of NU100P10, the 132 ppm band corresponding to the carbon atoms at the #2 position of PTCDA can be observed, indicating that the PTCDA framework remains intact (Wu et al., 2013).

The XPS determination was used to explore the chemical states of the NH_2-UiO-66/PTCDA system. As shown in Fig. 2a, according to the survey spectrum, C, N, O and Zr peaks mainly existed in the hybridized samples. As shown in Fig. 2b, the N 1s XPS spectrum of NU100P10 locating at 400.2 eV ascribed to the $-NH_2$ group due to amine functionalization. Compared with the pristine NH_2-UiO-66 (N 1s 399.8 eV), the N 1s peaks of NU100P10 only had a positive shift ascribing to the

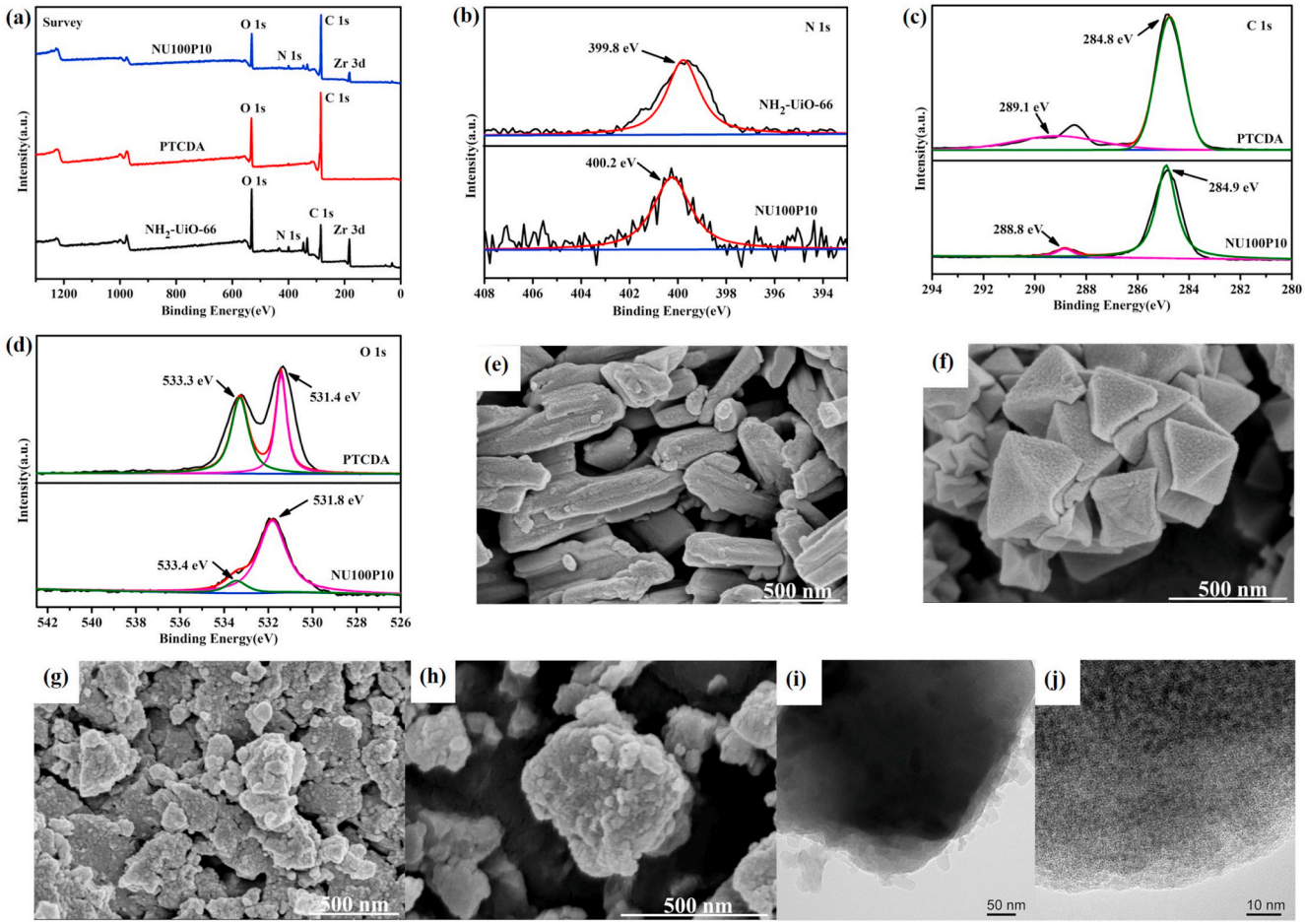

Fig. 2. (a) XPS survey spectrum of NH_2-UiO-66, PTCDA and NU100P10. (b) N 1s spectrum, (c) C 1s spectrum and (d) O 1s spectrum. The SEM images of (e) pristine PTCDA, (f) pristine NH_2-UiO-66, (g, h) NU100P10 composite and the HRTEM images of (i, j) NU100P10 composite.

strong electronic pull of the PTCDA that results in the deceased electron density of amino groups on NU100P10. It also indicates that the –O═C–N–C═O– bonds from imide ring of PI does not exist in NU100P10 (Wang et al., 2020b). The C 1s peak of NU100P10 in Fig. 2c appeared at 284.9 eV, which is in accordance with the form of sp^2 hybridized carbon, and another peak belonging to some oxygen-containing groups was present at 288.8 eV corresponding to the O–C═O bonds. The O 1s spectrum was shown in Fig. 2d. The peaks of NU100P10 centered at 531.8 and 533.4 eV assigned to the O–C and O═C bonds (Wang et al., 2017a; Zhang et al., 2019), respectively. After the combination of PTCDA and NH_2-UiO-66, the binding energy of O 1s corresponding to O–C was shifted from 531.4 eV to 531.8 eV. The above-stated shifts towards the high binding energy of O 1s in PTCDA were due to the change of electrons distribution in NU100P10 system, which confirmed the electrons transferred from PTCDA to NH_2-UiO-66 after their combination (Yi et al., 2019a).

The pristine PTCDA (Fig. 2e), individual NH_2-UiO-66 (Fig. 2f and NU100P10 (Fig. 2g and h) composite can be observed via SEM. The particle size of NH_2-UiO-66 ranged from 200 to 500 nm. After ball-milling, the PTCDA were coated onto the surface of NH_2-UiO-66. In order to understand the microscopic structure of the composites, more detailed investigations were conducted using HRTEM (Fig. 2i and j) and EDS elemental mapping (Fig. S4). Obviously, the observation revealed that the PTCDA are wrapped onto NH_2-UiO-66. The EDS element mapping images of NU100P10 composite in Fig. S4 demonstrated the relatively uniform distribution of C, N, O, and Zr.

3.2. Photocatalytic Cr(VI) reduction activities

3.2.1. Photocatalytic Cr(VI) reduction

The feasibility of photocatalytic reduction of Cr(VI) by all the photocatalysts were studied under visible light. All NU100P*X* composites showed higher reduction capacity toward Cr(VI) than the pure PTCDA and NH_2-UiO-66. The Cr(VI) in solution was completely removed by NU100P10 within 100 min (Fig. 3a). In addition, the pseudo-first order model was used to fit the kinetic plots of photocatalytic Cr(VI) reduction over NU100P*X* composites (Wang et al., 2016a). It can be observed that the photocatalyticreduction rates (*k* values) followed the order of NU100P10 > NU100P15 > NU100P5 > NU100P20 > NU100P3 > PTCDA > NH_2-UiO-66 (Fig. 3b). Based on the above-stated findings, the NU100P10 was selected as the optimal photocatalyst for further investigations.

To further evaluate the photocatalytic activities of NU100P10 under different monochromatic lights, the apparent quantum efficiencies (AQEs) towards the Cr(VI) reduction were tested. As displayed in Fig. S5, the AQEs of NU100P10 were 0.067%, 0.059%, 0.063%, 0.044% and 0.038% at 330 nm, 380 nm, 400 nm, 420 nm and 520 nm, respectively. The AQEs at different monochromatic lights were well consistent with the wavelength distribution of UV–vis DRS spectra, indicating that the Cr(VI) reduction over NU100P10 was a photocatalytic process (Li et al., 2020b).

3.2.2. Influence of initial pH

The adsorption and photocatalytic reduction performance of the photocatalysts for Cr(VI) were heavily influenced by different pH, as pH

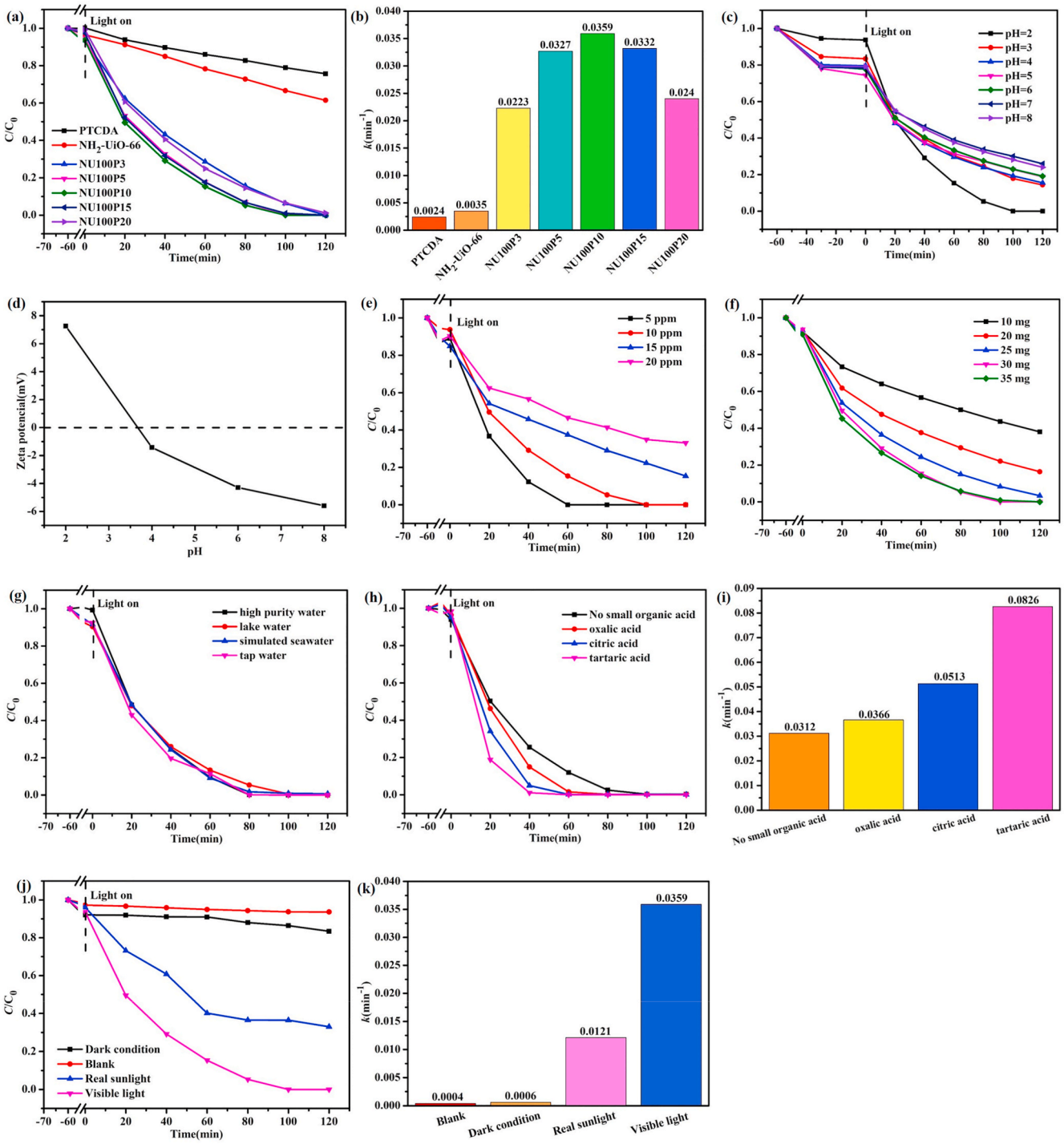

Fig. 3. (a) The photocatalytic Cr(VI) reduction over the samples under white light irradiation; (b) The photocatalytic Cr(VI) reduction rates (*k* values) over the different photocatalysts; (c) The effect of initial pH on Cr(VI) reduction and (d) Zeta potentials of NU100P10 under different pHs. The effect of different (e) initial Cr (VI) concentrations, (f) photocatalyst dosages, (g) water quality (lake/tap/simulated sea water), (h) hole scavengers on the photocatalytic Cr(VI) removal and (i) the *k* values over the different hole scavengers. (j) Photocatalytic Cr(VI) removal and (k) the photocatalytic Cr(VI) removal rates (*k* values) under different light sources. Conditions: NU100P10 = 30 mg, Cr(VI) = 10 mg L^{-1}, 80 mL, pH = 2.0. (Note: in Fig. 3g, the labels of "high purity water", "lake water" and "tap water" imply the Cr (VI) containing simulated wastewater samples formulated from ultrahigh water, lake water and tap water.).

can exert effect to the zeta potential of photocatalyst (Li et al., 2020a; Zhao et al., 2020) and the existence form of Cr(VI) (Guo et al., 2019). As shown in Fig. 3c and d, the zeta potential of NU100P10 was positive at pH = 2.0, while the adsorption towards Cr(VI) was lower than other pH values, indicating that the adsorption performances toward Cr(VI) could be contributed to electrostatic interactions and the amine groups on the surface of NU100P10 (Ahmadijokani et al., 2021). Nevertheless, the excessive Cr(VI) adsorption might mask the photoactive sites to inhibit the further Cr(VI) reduction. As illustrated in Fig. 3c, the photocatalytic Cr(VI) reduction efficiencies over NU100P10 increased obviously with the decreasing pH (100.0%, 82.1%, 80.6%, 77.2%, 77.0%, 69.9% and 71.8% at pH = 2.0, 3.0, 4.0, 5.0, 6.0, 7.0 and 8.0, respectively). In acidic environment, the transformation from Cr(VI) to Cr(III) over NU100P10 can be achieved by equation (2). The abundant H^+ was beneficial to the

transformation from Cr(VI) to Cr(III) in the form of $Cr_2O_7^{2-}$. However, under alkaline environment, CrO_4^{2-} is the main form of Cr(VI), and the photocatalytic reduction of Cr(VI) followed Eq. (3). In addition, the $Cr(OH)_3$ precipitate formed in an alkaline environment will cover the active sites of NU100P10, leading to poor photocatalytic Cr(VI) reduction performance.

$$Cr_2O_7^{2-} + 14H^+ + 6e^- \rightarrow 2Cr^{3+} + 7H_2O \quad (2)$$

$$CrO_4^{2-} + 4H_2O + 3e^- \rightarrow Cr(OH)_3 + 5OH^- \quad (3)$$

3.2.3. Influence of different initial Cr(VI) concentrations

The influence of initial Cr(VI) concentration was evaluated with C_0 being 5, 10, 15 and 20 mg L^{-1} respectively (Fig. 3e), in which it can be observed that the Cr(VI) reduction efficiency reduced as its initial concentration increases. The Cr(VI) removal efficiencies decreased from 100% at C_0 being 5 mg L^{-1} to 84.6% at C_0 being 10 mg L^{-1}, 62.5% at 15 mg L^{-1} and 53.4% at 20 mg L^{-1} within 60 min. It was deemed that the high concentration of pollutants leads to decreased catalytic efficiencies of the photocatalyst due to that the concentrated Cr(VI) might exerted mask over the active surface of the catalyst (Freudenhammer et al., 1997).

3.2.4. Influence of different photocatalyst dosages

As shown in Fig. 3f, the influences of photocatalyst dosages on Cr(VI) reduction were investigated by varying the dosages of NU100P10 as 10 mg, 20 mg, 25 mg, 30 mg and 35 mg. With increasing NU100P10 dosage, the removal efficiency of Cr(VI) increased from 62% to 100% due to more active sites for photocatalytic reactions (Zhang et al., 2017). When the dosage increased from 30 mg to 35 mg, the Cr(VI) reduction efficiency was not significantly improved. It is likely because the excessive particles might consequently hinder the light penetration (Meichtry et al., 2007).

3.2.5. Influence of various co-existing matters

The practicality of prepared photocatalysts were tested over NU100P10 under visible light. Different Cr(VI) aqueous solutions were prepared with tap water, lake water and simulated seawater. The concentration of the common cations and anions in the selected water samples can be found in Table S1. As shown in Fig. 3g, the Cr(VI) removal performances were hardly affected in simulated wastewater, indicating that the foreign co-existing ions did not exert noticeable inhibition towards the Cr(VI) reduction over NU100P10 photocatalyst.

3.2.6. Influence of various hole scavengers

To test the effect of consuming holes toward Cr(VI) removal, various small organic acids named oxalic acid, citric acid and tartaric acid were chosen as hole scavengers at pH being 2.0. As displayed in Fig. 3h, i, the photocatalytic Cr(VI) reduction performance was enhanced due to the existence of hole scavengers, following the order of tartaric acid (two α-hydroxyl groups) > citric acid (one α-hydroxyl groups) > oxalic acid (zero α-hydroxyl groups). The results were in consistent with the previous literatures (Rivero-Huguet and Marshall, 2009; Barrera-Díaz et al., 2012). The organic acids could be oxidized by photo-induced holes, resulting in the improved separation efficiency of photo-induced electron-hole pairs.

3.2.7. Photocatalytic performance under actual sunlight

As a green and sustainable light source, actual sunlight can be used for photocatalytic removal of Cr(VI). For photoactivity measurements of NU100P10 in a field experiment irradiated by real sunlight, photocatalytic removal of Cr(VI) was carried out at Daxing campus of BUCEA (39°44′ N, 116°17′E) in the winter season (November 29th, 2020, labeled as real sunlight, 3 °C) with the same experimental conditions as before. The spectrum of real sunlight and experimental details were illustrated in Figs. S6 and S7. In Fig. 3j, only 16.6% and 6.4% of Cr(VI) ions were removed by adsorption and without NU100P10 after 180 min under sunlight. The photocatalytic efficiency under real sunlight dropped to 67% due to the lower sunlight intensity. The average intensity of actual sunlight was 22.33 mW/cm^2, while the visible light intensity under experimental condition was just 28.66 mW/cm^2. As shown in Fig. 3k, the k values were 0.0006 min^{-1}, 0.0121 min^{-1} and 0.0359 min^{-1}, respectively, which were comparable to the previous reports (Zhao et al., 2019; Ren et al., 2020b).

3.2.8. Reusability and stability of NU100P10

In Fig. 4a, compared with the pure NH_2-UiO-66, after five cycles, the photocatalytic reduction of Cr(VI) performance of NU100P10 was still close to 100%, indicating that NU100P10 photocatalyst has excellent stability and efficiency. The PXRD patterns (Fig. 4b), FTIR (Fig. S8) and SEM (Fig. 4(c, d)) before and after five cycles proved the stability of NU100P10. As depicted in Fig. 4b, the material crystallinity was reduced, but the major XRD peaks still existed, indicating that the structure of the composite was not influenced (Wei et al., 2020). SEM images showed that NU100P10 remained the original morphologies (Chang, 2014). Additionally, FTIR analysis revealed no structural changes in NU100P10 after five cycles of photocatalytic operation (Su et al., 2019; Fakhri and Bagheri, 2020). It was well known that the MOFs like UiO-66 and NH_2-UiO-66 constructed from carboxylate ligands are stable under acidic conditions (Tambat et al., 2018), and the introduction of PTCDA can further strengthen the stability of NH_2-UiO-66.

3.2.9. The mechanism of photocatalytic Cr(VI) reduction

The photoluminescence (PL) and electrochemical impedance spectroscopy (EIS) measurements were applied to investigate the separation efficiency of photoinduced electron-hole pairs. NH_2-UiO-66, PTCDA and NU100P10 were excited at 350 nm (Zhou et al., 2019). The comparison for photoluminescence of NH_2-UiO-66, PTCDA and NU100P10 was displayed in Fig. 5a. The peak of NH_2-UiO-66 at 450 nm corresponds to the inter-band emission. The strong π-π stacking in PTCDA limits the low energy excitonic transition, which results in weak fluorescence of PTCDA. Compared with the pristine NH_2-UiO-66, the NU100P10 had a lower emission peak at 450 nm due to the effective charge transfer between NH_2-UiO-66 and PTCDA, which is in consistent with the peak of pristine PTCDA. In addition, time-resolved transient PL decay spectroscopy was a reasonable measurement for evaluating the separation efficiency of photo-induced e^- and h^+. As displayed in Fig. S9, the average PL lifetime ($\tau_{average}$) of the NU100P10 was 0.30 ns, while the $\tau_{average}$ of pure NH_2-UiO-66 and PTCDA were 0.28 ns and 0.26 ns. It is documented that the longer lifetime means the better separation efficiency of the photogenerated charge carriers in NU100P10 (Pan et al., 2012; Zhang et al., 2020a), which leads to the improved photocatalytic performance. To further investigate the photogenerated charge efficiency of NU100P*X* composites, the EIS measurements were conducted as illustrated in Fig. 5b. The arc radii followed the sequence of NH_2-UiO-66 > PTCDA > NU100P10, indicating that PTCDA/N-H_2-UiO-66 (NU100P*X*) composites show better photo–generated holes and electrons separation than the single NH_2-UiO-66 and PTCDA (Yuan et al., 2020). The photocurrent-time curves for the NH_2-UiO-66, PTCDA and NU100P10 were illustrated in Fig. S10. The photocurrent value of the NU100P10 was higher compared with those of pristine NH_2-UiO-66 and PTCDA, indicating more remarkable separation efficiency and prolonged lifetime of photo-generated carriers in NU100P*X* composites (Dai et al., 2015).

The formed active species over the NU100P10 were investigated according to the ESR tests (Fig. 5(c, d)). The notable ESR signals of both $\cdot O_2^-$ and ·OH are detected over NU100P10 at 5 min and 10 min' visible light irradiation. It proves the exist of both $\cdot O_2^-$ and ·OH in the system. In Fig. 5(e, f), the Mott-Schottky plots show that the flat band potentials of PTCDA and NH_2-UiO-66 are −0.37 eV and −1.05 eV versus AgCl/Ag electrode, respectively. In Fig. S11, the flat band potential of NU100P10

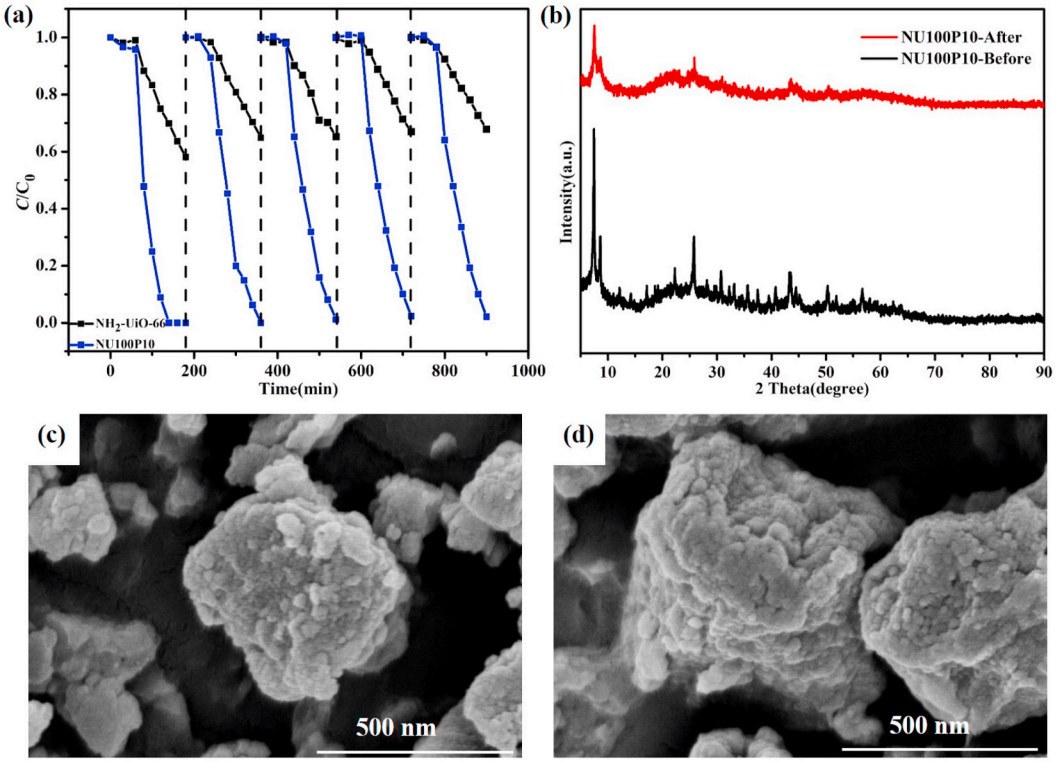

Fig. 4. (a) The cyclic tests for photocatalytic Cr(VI) removal over the pristine NH_2-UiO-66 and NU100P10; (b) PXRD patterns and (c, d) SEM images of NU100P10 before and after 5th cyclic experiments. Reaction conditions: NU100P10 dosage = 30 mg, Cr(VI) = 10.0 mg L^{-1}, pH = 2.0.

(- 1.05 eV) is similar to the LUMO potential of NH_2-UiO-66 (−1.05 eV) in the NU100P10 system (Wang et al., 2020b), which further indicates that the photogenerated electrons transfer from PTCDA to NH_2-UiO-66 after their combination. To further illustrate the direction of electron transfer, the cyclic voltammetry tests were conducted. As displayed in Fig. 5g, the oxidation potentials of PTCDA and NU100P10 were −0.25 V and −0.80 V, suggesting that PTCDA might be inclined to donate electrons to NH_2-UiO-66 in the NU100P10 composite (Wei and Zhu, 2019). Due to the potentials of PTCDA (VB, 1.89 eV *vs* NHE) and NH_2-UiO-66 (HOMO, 2.12 eV *vs* NHE) do not reach the standard potential (2.40 eV *vs* NHE) of the $OH^-/\cdot OH$ pairs, the photoinduced h^+ on the surface of PTCDA and NH_2-UiO-66 cannot react with H_2O to produce ·OH. Besides, the potential of LUMO (−0.85 eV *vs* NHE) of NH_2-UiO-66 is higher than that of $O_2/\cdot O_2^-$ pairs (−0.33 eV *vs* NHE). The electrons on LUMO can generate $\cdot O_2^-$ with the dissolved O_2 under acidic conditions.

It was generally to conduct DFT calculation to determine the electron mobility between two components in the composite (Ren et al., 2020a). According to the Bader charge analysis based on DFT calculation, the direction of electrons transfers between NH_2-UiO-66 and PTCDA within NU100P10 was clarified. As shown in Fig. 6a and b, the carbon, hydrogen, and oxygen atoms of PTCDA are represented by three colors of brown, white and red. The red and blue numbers respectively stand for positive and negative differential Bader charge values between PTCDA complexed with NH_2-UiO-66 and single PTCDA. It was found that the positive charge on the surface of PTCDA increased significantly, indicating that the electrons transferred from PTCDA to NH_2-UiO-66 within NU100P10 (Yi et al., 2019a). It is different from the model of perylene imide-modified NH_2-UiO-66 (PIU) (Wang et al., 2020b), in which partial electrons on the phenyl of H_2ATA move to perylene imide (PI) after modified by PTCDA.

To further certificate the electron transfer route, the photo-deposition of Pt nanoparticles were conducted for NU100P10. In most cases, Pt nanoparticles obtained from H_2PtCl_6 by accepting the electron can be used to confirm the direction of photo-generated electrons flow. As shown in Figs. S12a–c, no obvious lattice fringes could be observed in single PTCDA, while in the single NH_2-UiO-66 and NU100P10, the facet with lattice fringe spacing of 0.337 nm can be detected. In Fig. S12d, it was observed that Pt nanoparticles were deposited over NH_2-UiO-66 rather than PTCDA in NU100P10, which can be evidenced by the findings of lattice fringe spacing of 0.337 nm (NH_2-UiO-66) and 0.225 nm ((111) facet of Pt nanoparticle) (Jiang et al., 2018). The EDS elemental mapping of Pt nanoparticles on the NU100P10 in Fig. S13 further indicated that most of the Pt particles are deposited on the surface of NH_2-UiO-66. These results illustrated that the photo-generated electrons were transferred from PTCDA to NH_2-UiO-66, which was further affirmed both by the DFT calculation and cyclic voltammetry determination.

The radical quenching tests were conducted to study the contribution of various active species. EDTA-2Na and $KBrO_3$ were used as quenchers to trap holes and electrons. In Fig. 6c, the performances of Cr(VI) removal decreased obviously with the existence of $KBrO_3$, indicating that the electrons play a significant role towards the reduction of Cr(VI). The introduction of EDTA-2Na led to the improvement of Cr(VI) reduction ascribed to the better separation of photo-induced electrons. In addition, isopropyl alcohol (IPA) was introduced to the Cr(VI) reduction system. When ·OH has been captured by IPA, the Cr(VI) reduction performance decreased obviously, which was attributed to the shift of equilibrium in Eq. (8). The ·OH formation according to Eqs. (6) and (7) could exert influence on the reaction from Cr(V) back to Cr(VI) as displayed in Eq. (9). According to Eq. (4) and Eq. (5), $\cdot O_2^-$ as a mediator can transform Cr(VI) to Cr(V). As a result, nitrogen gas is introduced in the test to prevent the formation of $\cdot O_2^-$. In this work, the reduction of Cr(VI) over NU100P10 was significantly inhibited when there is N_2, which further shows that $\cdot O_2^-$ is also responsible for reducing Cr(VI).

$$O_2 + e^- \rightarrow \cdot O_2^- \quad (4)$$

$$\cdot O_2^- + Cr(VI) \rightarrow Cr(V) + O_2 \quad (5)$$

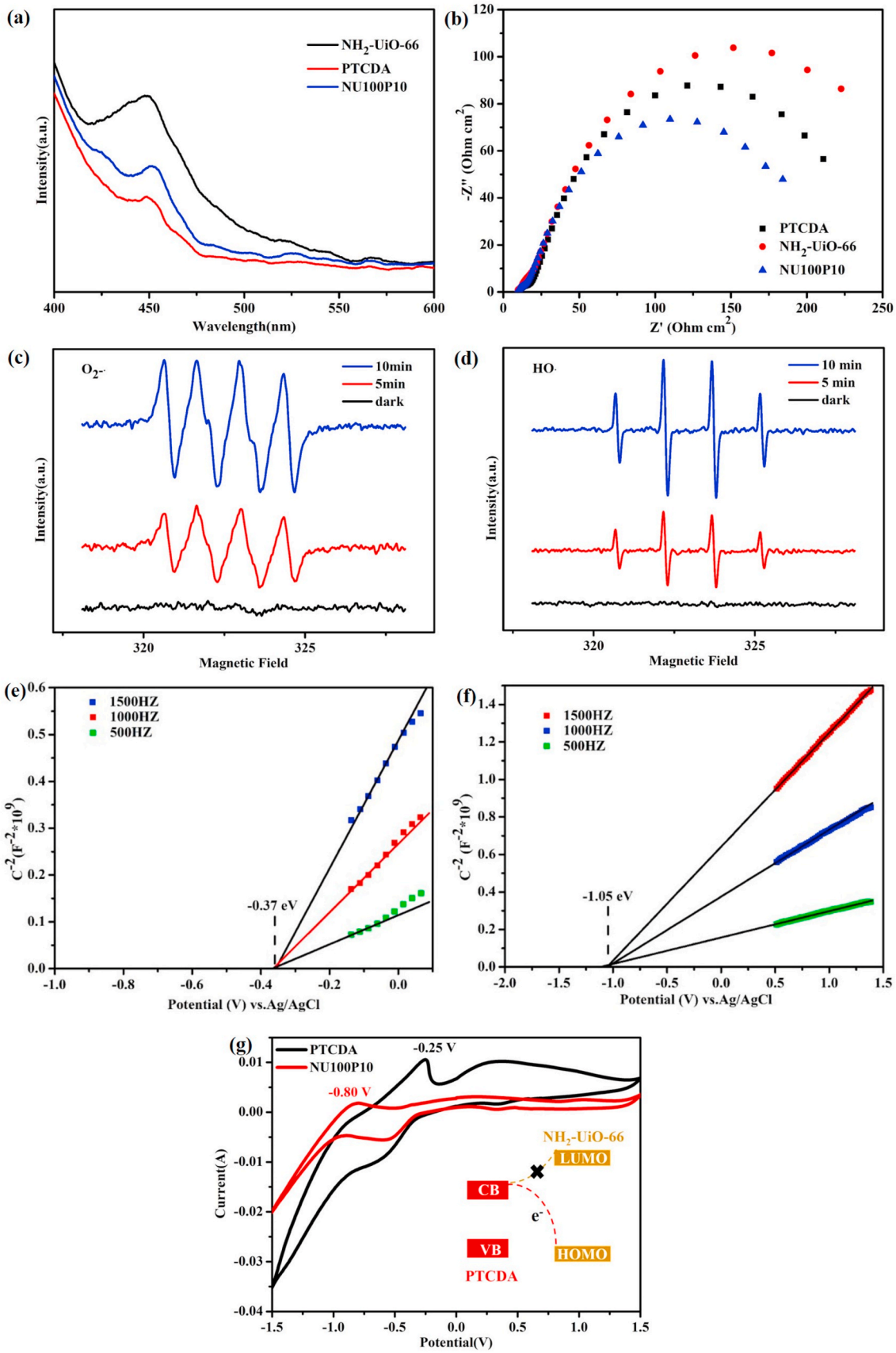

Fig. 5. (a) PL spectra of NH_2-UiO-66, PTCDA and NU100P10. (b) EIS of NU100P*X* composites. ESR spectra of different radicals trapped by DMPO for $\bullet O_2^-$ (c) and •OH (d) over NU100P10. The Mott–Schottky curves of (e) PTCDA and (f) NH_2-UiO-66 at various frequencies. (g) Cyclic voltammetry curves of PTCDA and NU100P10 in 0.2 M sodium sulfate solution with scanning rate of 10 mV s^{-1} from −1.5 V to 1.5 V.

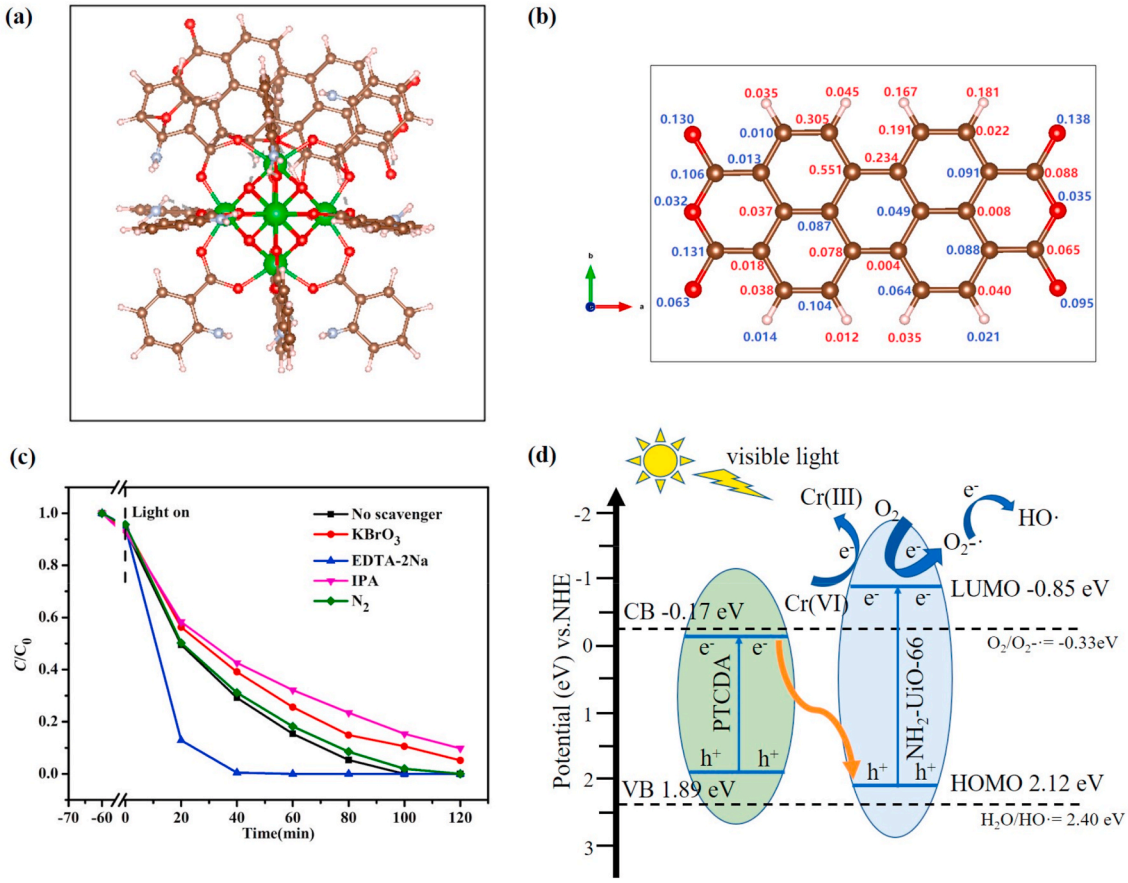

Fig. 6. (a) The structure of PTCDA on NH_2-UiO-66 surface after geometry relaxation. The green, brown, red, and white sphere represents Zr, C, O and H atom, respectively. (b) The change of Bader charge values between PTCDA complexed with NH_2-UiO-66 and PTCDA. The red and blue numbers stand for positive and negative differential Bader charge values, respectively. (c) The influences of various scavengers towards the Cr(VI) removal over NU100P10. (d) The proposed mechanism over NH_2-UiO-66/PTCDA as photocatalyst under visible light. (For interpretation of the references to color in this figure legend, the reader is referred to the Web version of this article.)

$$O_2 + 2H^+ + 2e^- \rightarrow H_2O_2 \quad (6)$$

$$H_2O_2 + e^- \rightarrow \cdot OH + HO^- \quad (7)$$

$$H_2O_2 + Cr(III) + H^+ \rightarrow Cr(VI) + H_2O + \cdot OH \quad (8)$$

$$Cr(V) + h^+/\cdot OH \rightarrow Cr(VI) + OH^- \quad (9)$$

According to the experimental results obtained, the Z-scheme mechanism over PTCDA/NH_2-UiO-66 is given in Fig. 6d, in which both pure PTCDA and NH_2-UiO-66 can be excited by visible light to produce photo-induced electrons and holes. The photo-generated holes prefer to retain in the VB of PTCDA, at the same time, the photo-induced e^- can migrate from the PTCDA's CB to the NH_2-UiO-66's HOMO, thereby improving the separation of photo-generated electrons and holes.

4. Conclusions

The NH_2-UiO-66/PTCDA (NU100P*X*) composite materials were prepared by simple mechanical ball-milling, in which the NU100P10 photocatalyst presented superior Cr(VI) sequestration efficiency to those of pristine PTCDA, NH_2-UiO-66 and other NU100P*X* under the irradiation of visible light. The PL analysis (including the time-resolved photoluminescence) and electrochemistry measurement indicated that the improved photocatalytic performances were mainly due to the enhanced photo-induced electrons motion over the interface of Z-scheme heterostructure. In addition, the effects of pH, initial Cr(VI) concentrations, real sunlight light, foreign ions and hole quenchers on photocatalytic Cr(VI) reduction were tested. According to the ESR and capture experiments, the main active substances to convert Cr(VI) into Cr(III) include e^- and $\cdot O_2^-$. Eventually, the cyclic experiments displayed that the NU100P10 composite had excellent stability and practicability. The Z-scheme mechanism was affirmed by the XPS determination, photo-deposition of Pt nanoparticles on NU100P10 and DFT calculation. This work further identified that the combination of MOFs and metal-free semiconductor PTCDA was a potential strategy for accomplishing enhanced photocatalytic performance.

Declaration of competing interest

The authors declare that they have no known competing financial interests or personal relationships that could have appeared to influence the work reported in this paper.

Acknowledgements

This work was supported by National Natural Science Foundation of China (51878023), Beijing Natural Science Foundation (8202016), Great Wall Scholars Training Program Project of Beijing Municipality Universities (CIT&TCD20180323), Beijing Talent Project (2020A27) and Fundamental Research Funds for Beijing Universities (X20147/X20141/X20106).

Appendix A. Supplementary data

Supplementary data to this article can be found online at https://doi.org/10.1016/j.chemosphere.2021.130734.

Author contribution statement

Xian Wei: Data curation, Investigation, Visualization, Writing – original draft. Chong-Chen Wang: Conceptualization, Funding acquisition, Supervision, Project administration, Writing – review & editing. Yang Li: Software, DFT calculation. Peng Wang: Resources. Qi Wei: Resources.

References

Ahmadijokani, F., Tajahmadi, S., Bahi, A., Molavi, H., Rezakazemi, M., Ko, F., Aminabhavi, T.M., Arjmand, M., 2021. Ethylenediamine-functionalized Zr-based MOF for efficient removal of heavy metal ions from water. Chemosphere 264, 128466.

Barrera-Díaz, C.E., Lugo-Lugo, V., Bilyeu, B., 2012. A review of chemical, electrochemical and biological methods for aqueous Cr(VI) reduction. J. Hazard Mater. 223, 1–12.

Butler, M., 1977. Photoelectrolysis and physical properties of the semiconducting electrode WO_2. J. Appl. Phys. 48, 1914–1920.

Chang, Y.-C., 2014. Low temperature growth of ZnO nanowire arrays with enhanced high performance photocatalytic activity and reusability. Catal. Commun. 56, 45–49.

Chen, D.-D., Yi, X.-H., Ling, L., Wang, C.-C., Wang, P., 2020a. Photocatalytic Cr(VI) sequestration and photo-Fenton bisphenol A decomposition over white light responsive PANI/MIL-88A(Fe). Appl. Organomet. Chem. 34, e5795.

Chen, D.-D., Yi, X.-H., Wang, C.-C., 2020b. Preparation of metal-organic frameworks and their composites using mechanochemical methods. Chinese J. Inorg. Chem. 36, 1805–1821.

Chen, D.-D., Yi, X.-H., Zhao, C., Fu, H., Wang, P., Wang, C.-C., 2020c. Polyaniline modified MIL-100(Fe) for enhanced photocatalytic Cr(VI) reduction and tetracycline degradation under white light. Chemosphere 245, 125659.

Chen, L., Ji, H., Qi, J., Huang, T., Wang, C.-C., Liu, W., 2021. Degradation of acetaminophen by activated peroxymonosulfate using $Co(OH)_2$ hollow microsphere supported titanate nanotubes: insights into sulfate radical production pathway through $CoOH^+$ activation. Chem. Eng. J. 406, 126877.

Dai, K., Lu, L., Liang, C., Zhu, G., Liu, Q., Geng, L., He, J., 2015. A high efficient graphitic-C_3N_4/BiOI/graphene oxide ternary nanocomposite heterostructured photocatalyst with graphene oxide as electron transport buffer material. Dalton Trans. 44, 7903–7910.

Daradmare, S., Xia, M., Kim, J., Park, B.J., 2021. Metal–organic frameworks/alginate composite beads as effective adsorbents for the removal of hexavalent chromium from aqueous solution. Chemosphere 270, 129487.

Dhakshinamoorthy, A., Li, Z., Garcia, H., 2018. Catalysis and photocatalysis by metal organic frameworks. Chem. Soc. Rev. 47, 8134–8172.

Du, X.-D., Yi, X.-H., Wang, P., Zheng, W., Deng, J., Wang, C.-C., 2019a. Robust photocatalytic reduction of Cr(VI) on UiO-66-NH_2 (Zr/Hf) metal-organic framework membrane under sunlight irradiation. Chem. Eng. J. 356, 393–399.

Du, X., Yi, X., Wang, P., Deng, J., Wang, C.-C., 2019b. Enhanced photocatalytic Cr(VI) reduction and diclofenac sodium degradation under simulated sunlight irradiation over MIL-100(Fe)/g-C_3N_4 heterojunctions. Chin. J. Catal. 40, 70–79.

Fakhri, H., Bagheri, H., 2020. Highly efficient Zr-MOF@WO_3/graphene oxide photocatalyst: synthesis, characterization and photodegradation of tetracycline and malathion. Mater. Sci. Semicond. Process. 107, 104815.

Freudenhammer, H., Bahnemann, D., Bousselmi, L., Geissen, S.-V., Ghrabi, A., Saleh, F., Si-Salah, A., Siemon, V., Vogelpohln, A., 1997. Detoxification and recycling of wastewater by solar-catalytic treatment. Water Sci. Technol. 35, 149–156.

Galán, B., Castañeda, D., Ortiz, I., 2005. Removal and recovery of Cr(VI) from polluted ground waters: a comparative study of ion-exchange technologies. Water Res. 39, 4317–4324.

Guo, J., Li, J.-J., Wang, C.-C., 2019. Adsorptive removal of Cr(VI) from simulated wastewater in MOF BUC-17 ultrafine powder. J. Environ. Chem. Eng. 7, 102909.

Hu, Q., Chen, Y., Li, M., Zhang, Y., Wang, B., Zhao, Y., Xia, J., Yin, S., Li, H., 2019. Construction of NH_2-UiO-66/BiOBr composites with boosted photocatalytic activity for the removal of contaminants. Colloid. Surface. Physicochem. Eng. Aspect. 579, 123625.

Jia, M., Yang, Z., Xu, H., Song, P., Xiong, W., Cao, J., Zhang, Y., Xiang, Y., Hu, J., Zhou, C., 2020. Integrating N and F co-doped TiO_2 nanotubes with ZIF-8 as photoelectrode for enhanced photo-electrocatalytic degradation of sulfamethazine. Chem. Eng. J. 388, 124388.

Jiang, W., Cai, Q., Xu, W., Yang, M., Cai, Y., Dionysiou, D.D., O'Shea, K.E., 2014. Cr(VI) adsorption and reduction by humic acid coated on magnetite. Environ. Sci. Technol. 48, 8078–8085.

Jiang, W., Zong, X., An, L., Hua, S., Miao, X., Luan, S., Wen, Y., Tao, F.F., Sun, Z., 2018. Consciously constructing heterojunction or direct Z-scheme photocatalysts by regulating electron flow direction. ACS Catal. 8, 2209–2217.

Li, K., Zhang, H., Tang, Y., Ying, D., Xu, Y., Wang, Y., Jia, J., 2015. Photocatalytic degradation and electricity generation in a rotating disk photoelectrochemical cell over hierarchical structured BiOBr film. Appl. Catal. B Environ. 164, 82–91.

Li, Y.-X., Han, Y.-C., Wang, C.-C., 2020a. Fabrication strategies and Cr(VI) elimination activities of the MOF-derivatives and their composites. Chem. Eng. J. 126648.

Li, Y.-X., Wang, X., Wang, C.-C., Fu, H., Liu, Y., Wang, P., Zhao, C., 2020b. Instrumental S-TiO_2/UiO-66-NH_2 composite for boosted photocatalytic Cr(VI) reduction and bisphenol A degradation under LED visible light. J. Hazard Mater. 399, 123085.

Meichtry, J.M., Brusa, M., Mailhot, G., Grela, M.A., Litter, M.I., 2007. Heterogeneous photocatalysis of Cr(VI) in the presence of citric acid over TiO_2 particles: relevance of Cr(V)–citrate complexes. Appl. Catal. B Environ. 71, 101–107.

Palansooriya, K.N., Yang, Y., Tsang, Y.F., Sarkar, B., Hou, D., Cao, X., Meers, E., Rinklebe, J., Kim, K.-H., Ok, Y.S., 2020. Occurrence of contaminants in drinking water sources and the potential of biochar for water quality improvement: a review. Crit. Rev. Environ. Sci. Technol. 50, 549–611.

Pan, C., Xu, J., Wang, Y., Li, D., Zhu, Y., 2012. Dramatic activity of C_3N_4/$BiPO_4$ photocatalyst with core/shell structure formed by self-assembly. Adv. Funct. Mater. 22, 1518–1524.

Radhika, S., Thomas, J., 2017. Solar light driven photocatalytic degradation of organic pollutants using ZnO nanorods coupled with photosensitive molecules. J. Environ. Chem. Eng. 5, 4239–4250.

Ren, K., Yu, J., Tang, W., 2020a. Two-dimensional ZnO/BSe van der waals heterostructure used as a promising photocatalyst for water splitting: a DFT study. J. Alloys Compd. 812, 152049.

Ren, X., Gao, M., Zhang, Y., Zhang, Z., Cao, X., Wang, B., Wang, X., 2020b. Photocatalytic reduction of CO_2 on BiOX: effect of halogen element type and surface oxygen vacancy mediated mechanism. Appl. Catal. B Environ. 274, 119063.

Rivero-Huguet, M., Marshall, W.D., 2009. Influence of various organic molecules on the reduction of hexavalent chromium mediated by zero-valent iron. Chemosphere 76, 1240–1248.

Su, Y., Wang, C., Zhang, Y., Yang, Z., Dionysiou, D.D., 2019. Design and preparation of SnO_2/SnS_2/conjugated polyvinyl chloride derivative ternary composite with enhanced visible-light photocatalytic activity. Mater. Res. Bull. 118, 110524.

Sukhanova, E., Popov, Z., Kvashnin, D., 2020. Theoretical study of the electronic and optical properties of a heterostructure based on PTCDA organic semiconductor and $MoSe_2$. JETP Lett. (Engl. Transl.) 111, 627–632.

Tambat, S.N., Sane, P.K., Suresh, S., Varadan, N., Pandit, A.B., Sontakke, S.M., 2018. Hydrothermal synthesis of NH_2-UiO-66 and its application for adsorptive removal of dye. Adv. Powder Technol. 29, 2626–2632.

Wang, C.-C., Du, X.-D., Li, J., Guo, X.-X., Wang, P., Zhang, J., 2016a. Photocatalytic Cr (VI) reduction in metal-organic frameworks: a mini-review. Appl. Catal. B Environ. 193, 198–216.

Wang, C., Niu, D., Liu, B., Wang, S., Wei, X., Liu, Y., Xie, H., Gao, Y., 2017a. Charge transfer at the PTCDA/black phosphorus interface. J. Phys. Chem. C 121, 18084–18094.

Wang, F.-X., Wang, C.-C., Wang, P., Xing, B.-C., 2017b. Syntheses and applications of UiO series of MOFs. Chin. J. Inorg. Chem. 33, 713–737.

Wang, H., Yuan, X., Wu, Y., Zeng, G., Chen, X., Leng, L., Wu, Z., Jiang, L., Li, H., 2015. Facile synthesis of amino-functionalized titanium metal-organic frameworks and their superior visible-light photocatalytic activity for Cr(VI) reduction. J. Hazard Mater. 286, 187–194.

Wang, J.-C., Ren, J., Yao, H.-C., Zhang, L., Wang, J.-S., Zang, S.-Q., Han, L.-F., Li, Z.-J., 2016b. Synergistic photocatalysis of Cr(VI) reduction and 4-Chlorophenol degradation over hydroxylated α-Fe_2O_3 under visible light irradiation. J. Hazard Mater. 311, 11–19.

Wang, J.-W., Qiu, F.-G., Wang, P., Ge, C., Wang, C.-C., 2020a. Boosted bisphenol A and Cr(VI) cleanup over Z-scheme WO_3/MIL-100(Fe) composites under visible light. J. Clean. Prod. 279, 123408.

Wang, J., Liu, X., Li, C., Yuan, M., Zhang, B., Zhu, J., Ma, Y., 2020b. Fabrication of perylene imide-modified NH_2-UiO-66 for enhanced visible-light photocatalytic degradation of tetracycline. J. Photochem. Photobiol. Chem. 401, 112795.

Wang, X., Li, Y.-X., Yi, X.-H., Zhao, C., Wang, P., Deng*, J., Wang, C.-C., 2021. Photocatalytic Cr(VI) elimination over BUC-21/N-$K_2Ti_4O_9$ composites: big difference in performances resulting from small difference in composition. Chin. J. Catal. 42, 259–270.

Wang, Y., Zhou, J., Hao, X., Wang, Y., Zou, Z., 2018. Fabricating direct Z-scheme PTCDA/g-C_3N_4 photocatalyst based on interfacial strong interaction for efficient photooxidation of benzylamine. Appl. Surf. Sci. 456, 861–870.

Wei, H., Hou, C., Zhang, Y., Nan, Z., 2017. Scalable low temperature in air solid phase synthesis of porous flower-like hierarchical nanostructure SnS_2 with superior performance in the adsorption and photocatalytic reduction of aqueous Cr(VI). Separ. Purif. Technol. 189, 153–161.

Wei, W., Zhu, Y., 2019. TiO_2@Perylene diimide full-spectrum photocatalysts via semi-core–shell structure. Small 15, 1903933.

Wei, X., Wang, P., Fu, H., Zhao, C., Wang, C.-C., 2020. Boosted photocatalytic elimination toward Cr(VI) and organic pollutants over BUC-21/$Cd_{0.5}Zn_{0.5}S$ under LED visible Light. Mater. Res. Bull. 129, 110903.

Weirsum, A., Lenoir, E., Yang, Q., Moulin, B., Guillerm, V., Yahia, M., Bourrelly, S., Vimont, A., Miller, S., Vagner, C., Daturi, M., Guillaume, C., Serre, C., Maurin, G., 2011. PL llewellyn. Chem. Asian J. 6, 3270–3280.

Wu, H., Wang, K., Meng, Y., Lu, K., Wei, Z., 2013. An organic cathode material based on a polyimide/CNT nanocomposite for lithium ion batteries. J. Mater. Chem. 1, 6366–6372.

Xia, S., Song, Z., Jeyakumar, P., Bolan, N., Wang, H., 2020. Characteristics and applications of biochar for remediating Cr(VI)-contaminated soils and wastewater. Environ. Geochem. Health 42, 1543–1567.

Xu, X.-Y., Chu, C., Fu, H., Du, X.-D., Wang, P., Zheng, W., Wang, C.-C., 2018a. Light-responsive UiO-66-NH_2/Ag_3PO_4 MOF-nanoparticle composites for the capture and release of sulfamethoxazole. Chem. Eng. J. 350, 436–444.

Xu, X.-Y., Zhang, J., Zhao, X., Fu, H., Chu, C., Wang, P., Wang, C.-C., 2018b. Visible-light-triggered release of sulfonamides in MOF/Ag-based nanoparticle composites: performance, mechanism, and DFT calculations. ACS Appl. Nano Mater. 2, 418–428.
Ye, C., Li, J.X., Wu, H.L., Li, X.B., Chen, B., Tung, C.H., Wu, L.Z., 2018. Enhanced charge separation efficiency accelerates hydrogen evolution from water of carbon nitride and 3,4,9,10-Perylene-tetracarboxylic dianhydride composite photocatalyst. ACS Appl. Mater. Interfaces 10, 3515–3521.
Yi, X.-H., Ma, S.-Q., Du, X.-D., Zhao, C., Fu, H., Wang, P., Wang, C.-C., 2019a. The facile fabrication of 2D/3D Z-scheme g-C_3N_4/UiO-66 heterojunction with enhanced photocatalytic Cr(VI) reduction performance under white light. Chem. Eng. J. 375, 121944.
Yi, X.H., Wang, F.X., Du, X.D., Wang, P., Wang, C.C., 2019b. Facile fabrication of BUC-21/g-C_3N_4 composites and their enhanced photocatalytic Cr(VI) reduction performances under simulated sunlight. Appl. Organomet. Chem. 33, e4621.
Yu, J., Xiong, W., Li, X., Yang, Z., Cao, J., Jia, M., Xu, R., Zhang, Y., 2019. Functionalized MIL-53(Fe) as efficient adsorbents for removal of tetracycline antibiotics from aqueous solution. Microporous Mesoporous Mater. 290, 109642.
Yuan, Y.-J., Shen, Z.-K., Wang, P., Li, Z., Pei, L., Zhong, J., Ji, Z., Yu, Z.-T., Zou, Z., 2020. Metal-free broad-spectrum PTCDA/g-C_3N_4 Z-scheme photocatalysts for enhanced photocatalytic water oxidation. Appl. Catal. B Environ. 260, 118179.
Zhang, F., Li, X., Zhao, Q., Chen, G., Zhang, Q., 2020a. High-performance In_2O_3@PANI core@shell architectures with ultralong charge carriers lifetime for photocatalytic degradation of gaseous 1,2-dichlorobenzene. Appl. Catal. B Environ. 263, 118278.
Zhang, F., Zhang, Y., Zhou, C., Yang, Z., Xue, H., Dionysiou, D.D., 2017. A new high efficiency visible-light photocatalyst made of SnS_2 and conjugated derivative of polyvinyl alcohol and its application to Cr(VI) reduction. Chem. Eng. J. 324, 140–153.
Zhang, S., Pei, X., Gao, H., Chen, S., Wang, J., 2020b. Metal-organic framework-based nanomaterials for biomedical applications. Chin. Chem. Lett. 31, 1060–1070.
Zhang, Z., Wang, S., Bao, M., Ren, J., Pei, S., Yu, S., Ke, J., 2019. Construction of ternary Ag/AgCl/NH_2-UiO-66 hybridized heterojunction for effective photocatalytic hexavalent chromium reduction. J. Colloid Interface Sci. 555, 342–351.
Zhao, C., Wang, J., Chen, X., Wang, Z., Ji, H., Chen, L., Liu, W., Wang, C.-C., 2020. Bifunctional $Bi_{12}O_{17}Cl_2$/MIL-100(Fe) composites toward photocatalytic Cr(VI) sequestration and activation of persulfate for bisphenol A degradation. Sci. Total Environ. 752, 141901.
Zhao, C., Wang, Z., Li, X., Yi, X., Chu, H., Chen, X., Wang, C.-C., 2019. Facile fabrication of BUC-21/$Bi_{24}O_{31}Br_{10}$ composites for enhanced photocatalytic Cr(VI) reduction under white light. Chem. Eng. J. 389, 123431.
Zhou, Y.-C., Wang, C.-C., Peng, W., Fu, H.-F., Zhao, C., 2020. In-situ photochemical reduction of Ag-UiO-66-NH_2 composite for enhanced photocatalytic performance. Chin. J. Inorg. Chem. 36, 2100–2112.
Zhou, Y.-C., Xu, X.-Y., Wang, P., Fu, H., Zhao, C., Wang, C.-C., 2019. Facile fabrication and enhanced photocatalytic performance of visible light responsive UiO-66-NH_2/Ag_2CO_3 composite. Chin. J. Catal. 40, 1912–1923.
Zhu, H., Huang, J., Zhou, Q., Lv, Z., Li, C., Hu, G., 2019. Enhanced luminescence of NH_2-UiO-66 for selectively sensing fluoride anion in water medium. J. Lumin. 208, 67–74.